

Modelling the Fluid Mechanics of Cilia and Flagella in Reproduction and Development

Thomas D. Montenegro-Johnson^{1,2}, Andrew A. Smith^{1,2}, David J. Smith^{1,2,3}, Daniel Loghin¹, and John R. Blake^{1,2}

¹*School of Mathematics, University of Birmingham, Edgbaston, Birmingham, B15 2TT, UK*

²*Centre for Human Reproductive Science, Birmingham Women's NHS Foundation Trust, Edgbaston, Birmingham, B15 2TG, UK*

³*School of Engineering & Centre for Scientific Computing, University of Warwick, Coventry, CV4 7AL, UK*

Abstract Cilia and flagella are actively bending slender organelles, performing functions such as motility, feeding and embryonic symmetry breaking. We review the mechanics of viscous-dominated microscale flow, including time-reversal symmetry, drag anisotropy of slender bodies, and wall effects. We focus on the fundamental force singularity, higher order multipoles, and the method of images, providing physical insight and forming a basis for computational approaches. Two biological problems are then considered in more detail: (1) left-right symmetry breaking flow in the node, a microscopic structure in developing vertebrate embryos, and (2) motility of microswimmers through non-Newtonian fluids. Our model of the embryonic node reveals how particle transport associated with morphogenesis is modulated by the gradual emergence of cilium posterior tilt. Our model of swimming makes use of force distributions within a body-conforming finite element framework, allowing the solution of nonlinear inertialess Carreau flow. We find that a three-sphere model swimmer and a model sperm are similarly affected by shear-thinning; in both cases swimming due to a prescribed beat is enhanced by shear-thinning, with optimal Deborah number around 0.8. The sperm exhibits an almost perfect linear relationship between velocity and the logarithm of the ratio of zero to infinite shear viscosity, with shear-thickening hindering cell progress. Montenegro-Johnson et al, Eur. Phys. J. E, 35 10 (2012) 111, published online: 29 October 2012 doi: 10.1140/epje/i2012-12111-1.

1 Introduction

The active locomotion of cells and transport of fluids on microscopic scales has been a benchmark problem in applied mathematics for the past 60 years, since Taylor [1] demonstrated that a two-dimensional sheet could swim utilising only viscous forces. The field had been an active area of research for zoologists for some time [2, 3, 4, 5], though a leap forward in understanding was made when experimentalists and theoreticians began to collaborate. It was in this spirit of collaboration, fostered by Taylor and Gray, that Hancock [6] first developed slender body theory, a powerful method based upon modelling slender swimmers by distributions of force singularities, which in turn has led to the development of the singularity methods used in the present study.

Microscale fluid propulsion is usually achieved in nature through the beating of cilia and flagella. These are

slender, hair-like organelles that perform a range of functions from locomotion to sensory reception. In reproduction, flagella propel sperm cells, allowing sperm and egg to meet, and cilia transfer the fertilised embryo from the ampulla to the uterus. Then, in the early stages of vertebrate embryonic development, cilia are responsible for the production of a directional fluid flow which breaks left-right symmetry in vertebrates [7]. This occurs in a fluid filled cavity that appears on the embryo shortly after fertilisation, called the node.

In eukaryotic cells, cilia and flagella induce active bending along their length via a remarkable, evolutionarily-conserved internal structure known as the *axoneme*, which was discovered with the advent of electron microscopy [8, 9, 10]. The axoneme comprises 9 inextensible outer microtubule doublets, as shown in fig. 1, and passive linking elements which stiffen the assembly. The combination of relative, localised microtubule sliding, their inextensibility

and the restraining effects of linking structures, generates bending. This is the ‘sliding filament theory’ first demonstrated by Satir [11]. For human sperm, as with most motile cilia and flagella, a central pair of microtubules runs along the length of the axoneme. This configuration is referred to as the “9+2” axoneme. Nodal cilia, however, lack this central pair. These “9+0” cilia were thought to be immotile until the relatively recent work of Nonaka *et al.* [7], which showed that they ‘whirled’ with a near rigid-body motion, quite distinct from the extensively studied beat patterns of 9+2 cilia.

In Newtonian fluids, such as sea water, microscopic cilia and flagella must execute a beat pattern that is not time reversible [12] in order to generate a net fluid flow. This is due to the lack of time dependence in the governing fluid equations, which are discussed in sect. 2. For sperm flagella, time reversibility is broken by propagating a bending wave along the length of the flagellum. However, nodal cilia are incapable of executing sophisticated waveforms, and so instead break symmetry by tilting their axis of rotation in a given direction. Hydrodynamic interaction with the cell wall then leads to an effective-recovery stroke asymmetry.

In this paper, we first summarise the fluid mechanics that govern the flow generated by cilia and flagella. We discuss the flow solution generated by a singular force, and the relationship between this fundamental solution and the physics governing the flow induced by the motion of slender bodies. We show how the effects of a no-slip wall may be incorporated through the inclusion of ‘image systems’ involving higher-order flow singularities, such as point stresses and torques. These are demonstrated graphically via singularity diagrams. We then discuss computational techniques that have arisen from modelling the action of cilia and flagella on the fluid by distributions of these flow singularities.

A combination of these computational techniques is used to model cilia-driven flow in the embryonic node in mice (fig. 2). The node is modelled at various stages of development, and the effects of posterior cilium tilt on the generation of directional flow is examined.

For many biological flow problems, for instance the swimming of sperm through cervical mucus, the assumption of Newtonian fluid rheology, as discussed in sect. 2, is invalid. In such cases, the fluid dynamics is governed by complicated nonlinear equations. We apply a finite element method developed by Montenegro-Johnson *et al.* [13] to an artificial swimmer described by Najafi and Golestanian [14], and examine the effects of nonlinear fluid rheology on the swimmer’s progression. We then apply the same techniques to model a two-dimensional analogue

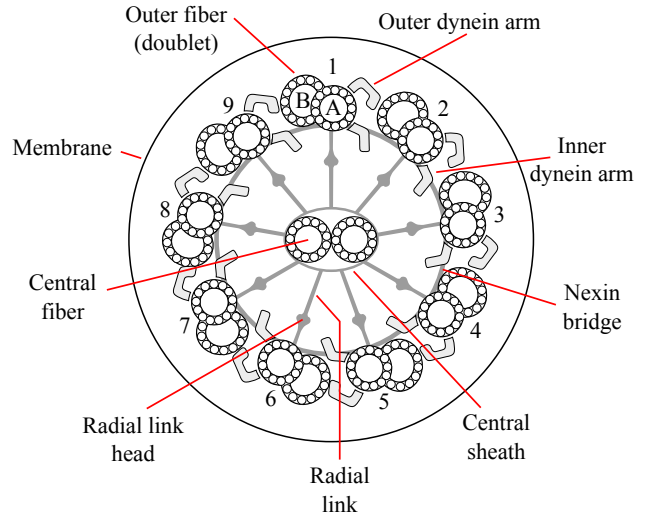


Figure 1: A schematic cross-section of the “9+2” axoneme, redrawn from Fawcett [15].

of human sperm.

2 Fluid mechanics of cilia and flagella

By considering the forces acting on an arbitrary volume of fluid and applying the laws of conservation of momentum and mass, we may derive the Cauchy equations

$$\rho \left(\frac{\partial \mathbf{u}}{\partial t} + (\mathbf{u} \cdot \nabla) \mathbf{u} \right) = \nabla \cdot \boldsymbol{\sigma} + \mathbf{F}, \quad (1a)$$

$$\frac{\partial \rho}{\partial t} + \nabla \cdot (\rho \mathbf{u}) = 0, \quad (1b)$$

Figure 2: Copyright figure available in published version. (a) Electron micrograph of a mouse embryo at 7.5 days post fertilisation, indicating the anterior-posterior and left-right directions (VN, ventral node; NP, notochordal plate; FG, foregut). Bar 100 μm , reprinted from Hirokawa *et al.* [16] (b) Cilia covering the nodal pit cells, reprinted from Nonaka *et al.* [17]. (c) Schematic figure showing a simplified model for nodal flow. Cilia rotate, with axis of rotation tilted towards the posterior, creating a right-to-left flow above the cilia tips. This is balanced by a return flow, due to the overlying Reichert’s membrane. The flow is believed to transport Nodal Vesicular Parcels (NVPs) which break up at the left of the node, delivering morphogen proteins to initiate asymmetric development.

which govern the motion of the fluid. Here, \mathbf{F} is the body force acting on the fluid, such as gravity, ρ is the fluid density and \mathbf{u} is the fluid velocity in a fixed frame of reference. The stress tensor $\boldsymbol{\sigma}$ incorporates the forces acting over the surface of an arbitrary parcel of fluid, such as pressure and internal friction, and is dependent on the type of fluid being modelled.

For Newtonian fluids, stress is proportional to strain rate, so that the fluid viscosity depends only on temperature, which is assumed to be constant throughout this study. In such cases,

$$\boldsymbol{\sigma} = -p\mathbf{I} + \frac{\mu}{2}\boldsymbol{\varepsilon}(\mathbf{u}), \quad (2)$$

for pressure, p and strain rate $\boldsymbol{\varepsilon}(\mathbf{u}) = \nabla\mathbf{u} + (\nabla\mathbf{u})^T$. A non-dimensionalisation of the Navier-Stokes equations that result from substitution of the stress (2) into the Cauchy momentum equation (1a) shows that the relative importance of viscous forces to inertial forces is given by the Reynolds number

$$\text{Re} = \frac{\rho U^2 L^2}{\mu U L} = \frac{\text{inertial force}}{\text{viscous force}}. \quad (3)$$

Fluid pumping and locomotion by microscopic cilia and flagella entails typical length-scales L of $\mathcal{O}(10^{-5} - 10^{-4})$ m and velocities U of $\mathcal{O}(10^{-5} - 10^{-4})$ m \cdot s $^{-1}$, with typical fluid densities around $\rho = \mathcal{O}(10^3)$ kg \cdot m $^{-3}$ and fluid viscosities of $\mu = \mathcal{O}(10^{-3})$ Pa \cdot s or greater. Thus, the Reynolds number of the flows we will consider is no higher than $\text{Re} = 10^{-2} \ll 1$, which indicates that viscous forces dominate over inertial forces. Thus, for Newtonian fluids, an accurate representation of the fluid mechanics is given by the Stokes flow equations,

$$\mu\nabla^2\mathbf{u} - \nabla p + \mathbf{F} = 0, \quad \nabla \cdot \mathbf{u} = 0. \quad (4)$$

2.1 The fundamental singularity

Insight into biological flows generated by cilia and flagella may be gained by considering the flows that arise due to concentrated driving forces. Consider an infinite fluid obeying the Stokes flow equations (4) that is driven by a concentrated force per unit volume $\mathbf{F} = \mathbf{f}\delta(\mathbf{x} - \mathbf{y})$, of magnitude and direction \mathbf{f} , where δ is the Dirac delta distribution centered at \mathbf{y} . The velocity solution corresponding to this fundamental singularity is given by

$$u_i(\mathbf{x}) = \frac{1}{8\pi\mu} \left(\frac{\delta_{ij}}{r} + \frac{r_i r_j}{r^3} \right) f_j(\mathbf{y}) = S_{ij}(\mathbf{x}, \mathbf{y}) f_j(\mathbf{y}), \quad (5)$$

where $r_i = x_i - y_i$ for $i = 1, 2, 3$, $r^2 = r_1^2 + r_2^2 + r_3^2$ and $S_{ij}(\mathbf{x}, \mathbf{y})$ is known as the Stokeslet, or Oseen-Burgers tensor. The Einstein summation convention applies throughout.

The anisotropy of the Stokeslet is an important factor affecting the fluid mechanics of cilia and flagella. As illustrated in fig. 3, the velocity of the flow due to a singular force, at a distance r_1 from the force, is twice as large at points in line with the force than at those points perpendicular to the force at the same distance. As a first approximation, the action of a slender cylinder moving through a fluid may be represented by a line distribution of singular driving forces, as shown in fig. 3. Since the Stokes flow equations (4) are linear, the corresponding velocity field is given by a sum of Stokeslet solutions. Thus, the drag on a slender body moving tangentially through the flow is approximately half that on an equivalent body moving normally. This ‘‘two to one ratio’’, first described in the resistive force theory of Gray and Hancock [18] is the basis for flagella and ciliary propulsive dynamics. However, drag anisotropy is not itself essential for very low Reynolds number propulsion if the filaments are extensible, as recently shown by Pak & Lauga [19].

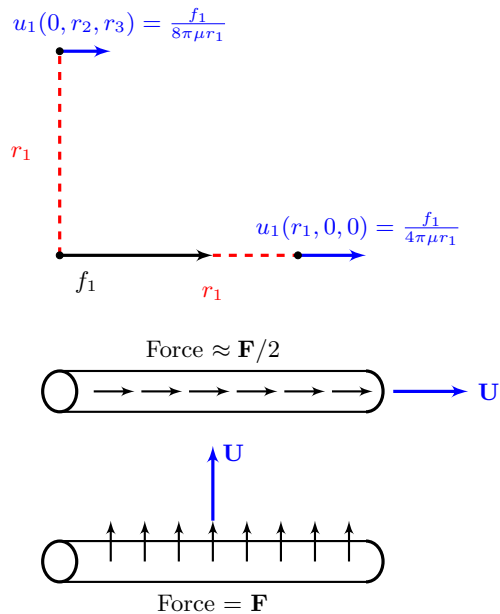


Figure 3: The flow generated by a singular force, and a demonstration of the 2:1 drag anisotropy that enables flagellar and ciliary propulsion, redrawn from Blake and Sleigh [20].

Swimmers in Stokes flow move in such a way that no net forces [1] or torques [21] act upon them, and flows driven by cilia protruding from epithelia can be modelled with image systems, as discussed in sect. 2.2. In both cases, the

far-fields of the flow are given by higher-order singularities. By taking derivatives of the Stokeslet, it is possible to derive the flow fields generated by higher-order singularities, such as point stresses and point torques. These are able to provide valuable insight into the far-field behaviour of the fluid surrounding swimming cells, and into the hydrodynamic effects arising from the inclusion of no-slip boundaries in the flow [22, 23]. Fig. 4 shows the schematic representation of some of these singularities.

With each increase in the order of singularity, the decay of the fluid velocity in the far-field is increased by $\mathcal{O}(1/r)$, so that Stokeslets decay with $\mathcal{O}(1/r)$, stokes dipoles decay with $\mathcal{O}(1/r^2)$ and stokes quadrupoles with $\mathcal{O}(1/r^3)$.

An additional important singularity, familiar as the source dipole of potential flow theory, is given by,

$$D_{ij}(\mathbf{x}, \mathbf{y}) = -\frac{1}{4\pi} \left(\frac{\delta_{ij}}{r^3} - \frac{3r_i r_j}{r^5} \right). \quad (6)$$

This expression for the i -component of a velocity field due to a source dipole oriented in the j -direction, together with zero pressure field, is also a solution of the Stokes flow equations, and can be combined with the Stokeslet to formulate solutions for translating spheres, ellipsoids and slender rods. The source dipole can alternatively be identified as the Laplacian of the Stokeslet—in other words, a particular form of the stokes quadrupole.

Singularity models capture many of the essential features of cilia and flagella driven flows. Fig. 5 shows experimental data from recent studies by Drescher *et al.* [24, 25]. Sperm, bacteria and individual algae are too small for gravitational sedimentation to have a dominant effect on the flow field; the zero total force condition therefore entails that the far-field is given by a stresslet (fig. 5a). Simulation modelling (fig. 6) predicts that the flow field around a sperm is approximated well by a stokes quadrupole, given by drag components at the front and rear of the cell and a propulsive component in the middle; sufficiently far from the cell the dominant singularity will however still be the stresslet.

The flow field closer to the cell is more complex; for biflagellate algae the time averaged flow field due to two propulsive flagella and the cell body can be represented by a three Stokeslet model [24] (fig. 5b). Larger swimmers such as *Volvox Carteri* colonies are subject to a significant gravitational force, evident as a Stokeslet far-field (fig. 5c); the near-field is given by a source dipole and stresslet combination (fig. 5d).

2.2 Wall effects

The presence of a rigid boundary near a Stokeslet significantly alters the resultant flow field. This may be un-

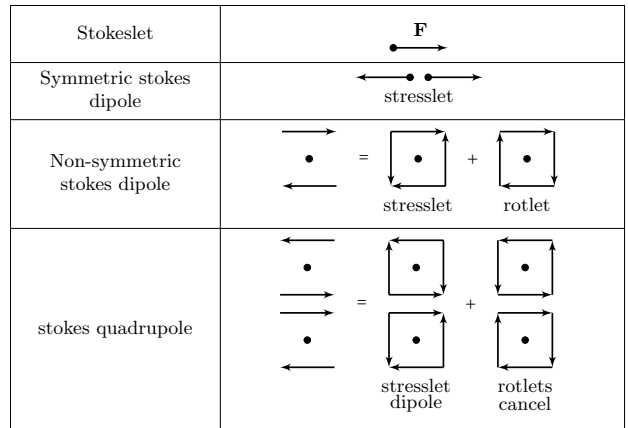


Figure 4: Singularities of Stokes flow, with forces represented by arrow vectors. Displaced forces represent higher order singularities.

Figure 5: Copyright figure available in published version. (a) Experimentally observed stresslet behaviour in the far-field of a swimming bacterium [25] (b) Experimentally observed flow field around a swimming biflagellate *Chlamydomonas Reinhardtii*, showing that the data are fitted accurately by a three-Stokeslet model [24] (c,d) Experimentally observed flow fields around a larger swimmer, the *Volvox Carteri* algal colony [24]. The larger swimmer is subject to a non-negligible gravitational force, evident as a far-field Stokeslet. (d) Shows the near-field when the Stokeslet field is subtracted, observed to resemble a source dipole and stresslet [24]

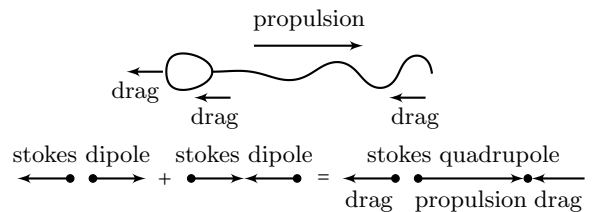


Figure 6: An approximate singularity representation of the flow field surrounding a human sperm, redrawn from Smith and Blake [26]. The quadrupole representation was suggested after calculation of the force distribution in the tail with slender body theory.

derstood through the use of singularity diagrams. To enforce the zero velocity condition on the plane boundary, that may for example represent the nodal floor, an image system of singularities is placed the other side of the boundary [22]. The explicit form for the velocity field arising from a point force located at height h above a plane boundary represented by image systems is,

$$B_{ij}(\mathbf{x}, \mathbf{y}) = \frac{1}{8\pi\mu} \left[\left(\frac{\delta_{ij}}{r} + \frac{r_i r_j}{r^3} \right) - \left(\frac{\delta_{ij}}{R} + \frac{R_i R_j}{R^3} \right) + 2h\Delta_{jk} \frac{\partial}{\partial R_k} \left\{ \frac{hR_i}{R^3} - \left(\frac{\delta_{i3}}{R} + \frac{R_i R_3}{R^3} \right) \right\} \right]. \quad (7)$$

The tensor Δ_{jk} takes value +1 for $j = k = 1, 2$, value -1 for $j = k = 3$, and zero if $j \neq k$. The image location is given by $R_1 = r_1$, $R_2 = r_2$ and $R_3 = -h$.

The image systems for the two cases corresponding to a force orientated parallel and perpendicular to the boundary are shown in fig. 7. The far-field arising from a Stokeslet near a plane boundary is of higher order than the corresponding Stokeslet in an infinite fluid, being $\mathcal{O}(1/r^2)$ in the parallel case and $\mathcal{O}(1/r^3)$ for the perpendicular case. The boundary therefore has the effect of shielding the fluid in the far-field from the effect of the Stokeslet. It is this shielding effect, illustrated in fig. 8, that allows nodal cilia to generate directional fluid flow by tilting their axis of rotation in the posterior direction in mice [27]; we will investigate the resultant fluid mechanics in more detail in sect. 3.

Figure 7: Copyright figure available in published version. A diagram illustrating the image systems for a Stokeslet orientated parallel (a) and perpendicular (b) to a no-slip plane boundary. Note that the wall induces a more rapid decay in the far-field, which is of $\mathcal{O}(1/r^2)$ in the parallel case and $\mathcal{O}(1/r^3)$ in the perpendicular case. [28, fig. 4(a,b)]

Figure 8: The *wall effect*: the zones of influence of a whirling nodal cilium protruding from a cell surface during (a) the effective stroke and (b) the recovery stroke. The far-field strength decays more rapidly than the inner- and near-fields due to the wall influence; moreover, during the effective stroke, the cilium is further from the cell surface than during the recovery stroke, resulting in the near-field having greater extent, and propelling more fluid. This effective-recovery stroke asymmetry results in net fluid propulsion in the direction of the effective stroke.

For further detailed review of low Reynolds number biofluidynamics, see Dillon *et al.* [29], Lauga and Powers [30] and Gaffney *et al.* [31]. We now consider two problems which can be analysed using singularity approaches. For the first, Newtonian symmetry-breaking flow in the node, we apply slender body theory and the method of regularised Stokeslets to model the cilia and the node geometry respectively, discussed in sect. 3. For the second, swimming in non-Newtonian fluids, we use a recently developed hybrid of singularity methods with the finite element method [13], which we have dubbed the ‘method of femlets’, discussed in sect. 4.

3 Nodal cilia

Embryonic nodal cilia were first discovered in the 1990s, and a series of experimental studies confirmed that cilia motility produced a fluid flow essential for the breaking of left-right symmetry, resulting in the normal asymmetric placement of the internal organs in vertebrates. One of the most remarkable aspects of this work was the resolution of the long standing clinical question of how cilia dysfunction and *situs inversus*, reversal of the internal body plan, often appear together [32, 33]. In this section we review recent fluid mechanical models of this process, before presenting new results inspired by recent biological observations on the developmental progression of cilia placement and configuration.

3.1 Geometry of the embryonic mouse node

Vertebrate development requires the establishment of three body axes. In order of appearance they are: dorsal-ventral, anterior-posterior, and left-right. Following a series of experimental studies, it is now known that cilia motion converts the already-established anterior-posterior axis information with an intrinsic chirality [34], i.e. rotational direction, into left-right asymmetric flow. Cilia perform a ‘whirling’ clockwise motion, viewed tip-to-base, with axis of rotation tilted towards the posterior. This model was first advanced by Cartwright *et al.* [35], with the fluid mechanics of cell surface interaction being discussed by Brokaw [36] and analysed in more detail by Smith *et al.* [28, 27, 37]. Hashimoto *et al.* [38] established that the posterior tilt is generated because the basal body of the cilium migrates towards the posterior side of the convex cell surface.

This process takes place in the ventral node, shown in fig. 2. In the most extensively-studied species, the mouse, the node is an approximately triangular depression measuring 50–100 μm in width and 10–20 μm in depth [32], forming on the ventral side of the embryo at 7–9 days post-fertilisation (dpf). The node is covered with a membrane

and filled with extraembryonic fluid, which we model as Newtonian, motivating an approach based on the Stokes flow theory described in sect. 2. The dorsal surface of the node is covered with a few hundred nodal pit cells that typically have one or two cilia protruding from them into the node. Each cilium is approximately $3\text{--}5\ \mu\text{m}$ in length and $0.3\ \mu\text{m}$ in diameter.

Hashimoto *et al.* [38] characterised morphological changes during the developmental process that primarily affect cilia numbers and positions, which we summarise briefly: at the *late bud* stage, occurring at approximately 7.5–8 dpf (for details of developmental stages, see Downs & Davies [39]), cilia exhibit a distribution of tilt angle, but no overall bias. At a slightly later stage of development, *early headfold*, also occurring in the period approximately 7.5–8 dpf and subsequently *late headfold*, at approximately 8 dpf, cells exhibit a significant posterior bias, and a significantly greater posterior bias in the peripheral regions relative to the centre. In the later developmental stages known as *1 somite* and *3 somite*, occurring at approximately 8 dpf, posterior tilted cilia are extremely dominant.

During development, cilia migrate towards the posterior side of the nodal pit cell, which results in an increase of tilt angle in the posterior direction. These features will be modelled using different sets of cilia positions and parameters. As observed by Hashimoto *et al.* [38] certain mutant embryos with *Dvl1*, *Dvl2*, *Dvl3* genes ‘knocked out’ do not exhibit cilia migration and consequently do not produce a directional fluid flow. The experimental study of Hashimoto *et al.* provides information on instantaneous slices of the two-dimensional flow fields using microscopic particle imaging velocimetry and how this is altered by genetic knockouts; a complementary technique to study the flow generation and the influence of cilia tilt is to formulate a mathematical model, allowing the prediction of features which are not yet available experimentally, for example three-dimensional particle tracks. We will describe briefly a computation model of Stokes flow generated by tilted rotating cilia published previously [28] and then apply the model to interpret the fluid mechanics of the changing developmental stages described by Hashimoto *et al.*

3.2 Modelling the stages of development in the embryonic mouse node

We will represent the ciliated surface, or nodal floor, by the plane $x_3 = 0$ with cilia protruding into the region $x_3 > 0$. The x_1 -axis will correspond to the left-right axis, with positive x_1 being towards the ‘left’, and the x_2 -axis will be the anterior-posterior axis, with negative x_2 being

towards the posterior. In this configuration, posterior tilt corresponds to the negative x_2 -direction.

Each cilium is tilted towards the already-established posterior direction by an angle θ and performs a conical rotation with semi-cone angle ψ and angular frequency ω . The centreline at arclength s and time t is therefore given by

$$\xi_1(s, t) = s \sin \psi \cos(\omega t), \quad (8a)$$

$$\xi_2(s, t) = s(-\sin \psi \sin(\omega t) \cos \theta - \cos \psi \sin \theta), \quad (8b)$$

$$\xi_3(s, t) = s(-\sin \psi \sin(\omega t) \sin \theta + \cos \psi \cos \theta), \quad (8c)$$

with the restriction $\theta + \psi < 90^\circ$ so that each cilium does not come into contact with the ciliated surface, see fig. 9. The slenderness ratio is defined as $\eta = a/L$, where a is the cilium radius and L is the cilium length. For nodal cilia η is approximately 0.1. The relative slenderness of the cilium indicates that slender body theory can be used to represent both the near- and far-field flows accurately, however it is also necessary to take into account both the no-slip condition on the plane boundary representing the ciliated surface, and the membrane that encloses the node, known as *Reichert’s membrane*.

Figure 9: Copyright figure available in published version. The configuration of a tilted straight rod by an angle of θ , where ψ is the semi-cone angle. Axis notation, V, ventral; A, anterior; P, posterior; L, left and R, right.

The no-slip condition on the plane boundary is satisfied through the Stokeslet and image system given in eq. (7). The no-slip condition on the cilium is satisfied by a Stokeslet and quadratically-weighted source dipole distribution. In this formulation the surface of a cilium is modelled as a slender prolate ellipsoid given by,

$$\mathbf{X}_\alpha(s, t) = \boldsymbol{\xi}(s, t) + a \sqrt{1 - \frac{(s-1/2)^2}{a^2 + 1/4}} (\mathbf{n}(s, t) \cos \alpha + \mathbf{b}(s, t) \sin \alpha). \quad (9)$$

The vectors $\mathbf{n}(s, t)$ and $\mathbf{b}(s, t)$ are normal and binormal respectively, the azimuthal angle α ranges from 0 to 2π , and $\boldsymbol{\xi}(s, t)$ is the straight centreline of the ellipsoid defined by eq. (8). To ensure that $u_i(\mathbf{X}_\alpha(s_0, t)) \approx \partial_t \xi_i(s_0, t)$ uniformly, including towards the cilium ends and for all α , we combine a centreline distribution of Stokeslets with a quadratically-weighted distribution of source dipoles [40].

The flow due to a single cilium \hat{u}_i is then represented

by the integral equation,

$$\hat{u}_i(\mathbf{x}, t) = \int_0^1 [B_{ij}(\mathbf{x}; \boldsymbol{\xi}(s, t))f_j(s, t) + D_{ij}(\mathbf{x}; \boldsymbol{\xi}(s, t))g_j(s, t)] ds. \quad (10)$$

The function $f_j(s, t)$ is the force per unit length on a cilium and $g_j(s, t)$ is a source dipole distribution. An image system is not required for the source dipole because the additional terms needed to satisfy the no-slip condition decay rapidly; an expression for the source dipole image system can also be derived [41]. The source dipole distribution, originally derived by Chwang & Wu [42] in the context of exact solutions to Stokes flow and later found asymptotically by Johnson [40], takes the form

$$g_j(s, t) = -\frac{a^2 s(1-s)}{\mu} f_j(s, t). \quad (11)$$

Due to the linearity of Stokes' equations the contribution to the velocity field from each cilium is given by the sum of slender body integrals,

$$u_i^{\text{cilia}}(\mathbf{x}, t) = \sum_{m=1}^M \int_0^L G_{ij}(\mathbf{x}, \boldsymbol{\xi}^{(m)}(s, t)) f_j^{(m)}(s, t) ds + \mathcal{O}(\eta^2). \quad (12)$$

The total number of cilia is denoted by M , the parameter L is the length of each cilium, and the Green's function $G_{ij} = B_{ij} - a^2 s(1-s)D_{ij}/\mu$ is a combination of Stokeslet and plane boundary image system with the quadratically-weighted source dipole. The no-slip condition on the surface of each cilium is preserved provided that the cilia do not approach each other too closely, a satisfactory approximation for nodal cilia [27]. The centreline of the m th cilium is denoted $\boldsymbol{\xi}^{(m)}(s, t)$, defined by eq. (8) with a range of base positions. The a priori unknown force per unit length on the m^{th} cilium is denoted $f_j^{(m)}(s, t)$.

To incorporate the covering membrane of the mouse node a surface mesh of a cube is rearranged into a smooth, approximately triangular shape S , as described in Smith *et al.* [28] and shown in fig. 10. The contribution to the velocity field from the membrane can be approximated by a single-layer boundary integral of regularised Stokeslets and plane boundary images over the membrane surface S . To obtain a regular flow field throughout domains containing singularity distributions, Cortez [43] developed the method of regularised Stokeslets. A regularised Stokeslet is defined as the exact solution to eq. (4) where \mathbf{F} is given as a smoothed point-force, $\mathbf{F} = \mathbf{f}\psi_\epsilon(\mathbf{x} - \mathbf{y})$. The symbol $\psi_\epsilon(\mathbf{x} - \mathbf{y})$ denotes a cut-off function with regularisation parameter ϵ . For the choice $\psi_\epsilon(\mathbf{x} - \mathbf{y}) = 15\epsilon^4/(8\pi\mu r_\epsilon^7)$,

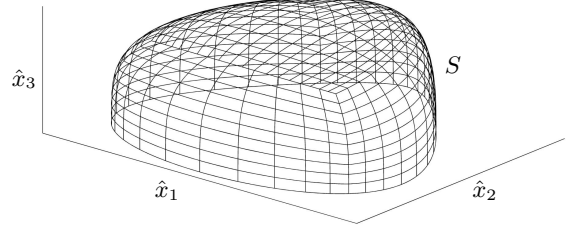


Figure 10: A view of the mesh used to enclose the node denoted by S . The \hat{x}_1 axis represents the left-right axis with positive \hat{x}_1 being towards the left of the embryo. The \hat{x}_2 axis represents the anterior-posterior axis with negative \hat{x}_2 being towards the posterior. The \hat{x}_3 axis represents the dorsal-ventral axis with positive \hat{x}_3 being the ventral direction.

Cortez *et al.* [44] showed that the regularised Stokeslet has the form,

$$S_{ij}^\epsilon(\mathbf{x}, \mathbf{y}) = \frac{1}{8\pi\mu} \left(\frac{\delta_{ij}(r^2 + 2\epsilon^2) + r_i r_j}{r_\epsilon^3} \right), \quad (13)$$

where $r_\epsilon^2 = r^2 + \epsilon^2$ and the velocity due to a regularised Stokeslet in an infinite domain is then $u_i = S_{ij}^\epsilon f_j$. Ainley *et al.* [45] then derived the regularised image system Stokeslet that satisfies the no-slip boundary condition which can be written in index notation for a plane boundary at $x_3 = 0$ as

$$B_{ij}^\epsilon(\mathbf{x}, \mathbf{y}) = \frac{1}{8\pi\mu} \left(\frac{\delta_{ij}(r^2 + 2\epsilon^2) + r_i r_j}{r_\epsilon^3} - \frac{\delta_{ij}(R^2 + 2\epsilon^2) + R_i R_j}{R_\epsilon^3} + 2h\Delta_{jk} \left[\frac{\partial}{\partial R_k} \left\{ \frac{hR_i}{R_\epsilon^3} - \frac{\delta_{i3}(R^2 + 2\epsilon^2) + R_i R_3}{R_\epsilon^3} \right\} - 4\pi h\delta_{ik}\phi_\epsilon(R) \right] - \frac{6h\epsilon^2}{R_\epsilon^5} (\delta_{i3}R_j - \delta_{ij}R_3) \right) \quad (14)$$

where $R_\epsilon^2 = R^2 + \epsilon^2$, $\phi_\epsilon(R) = 3\epsilon^2/(4\pi R_\epsilon^5)$ and Δ_{jk} has the same definition as in eq. (7). The velocity contribution from the covering membrane is then,

$$u_i^{\text{mem}}(\mathbf{x}, t) = \iint_S B_{ij}^\epsilon(\mathbf{x}, \mathbf{y}) \phi_j(\mathbf{y}, t) dS_{\mathbf{y}} + \mathcal{O}(\epsilon^2), \quad (15)$$

with $\phi_j(\mathbf{y}, t)$ the unknown j^{th} component of the stress on the membrane at \mathbf{y} and ϵ a regularisation parameter, in this case chosen to be $0.06L$ (for further details, see references [28, 43, 44, 45, 46]). An advantage of a regularised Stokeslet formulation in this context is that the velocity

field near to, and on, the surface S is regular, and can be calculated using Gauss-Legendre quadrature.

The velocity in the domain can then be written as the sum,

$$u_i(\mathbf{x}, t) = \iint_S B_{ij}^c(\mathbf{x}, \mathbf{y}) \phi_j(\mathbf{y}, t) dS_{\mathbf{y}} + \mathcal{O}(\epsilon^2) + \sum_{m=1}^M \int_0^L G_{ij}(\mathbf{x}, \boldsymbol{\xi}^{(m)}(s, t)) f_j^{(m)}(s, t) ds + \mathcal{O}(\eta^2). \quad (16)$$

It remains to approximate the unknown stress distribution $\phi_j(\mathbf{y}, t)$ and force per unit length distribution $f_j^{(m)}(s, t)$ for each timestep comprising a beat cycle. This is achieved by imposing the no-slip condition at discrete points on each cilium and the surface mesh, and using a boundary element constant force discretisation; for full details of the numerical implementation, see refs. [28, 46]. Once the stress and force per unit length distributions are known, it is then possible to calculate the fluid velocity from eq. (16); knowledge of the velocity field then enables simulation of particle transport.

3.3 Configurations of cilia during development

Since computational expense grows approximately with the cube of the number of cilia, we model the node with a smaller number of cilia than are observed experimentally. However, the underlying characteristics of the problem such as tilt direction and the geometry of the problem domain will be preserved.

Building on the work of Smith *et al.* [28], we will focus on the stages of development where the fluid flow appears to change from vortical to directional; the stages considered are the late bud, early headfold, late headfold, 1 somite and 3 somite. For the late bud stage 17 cilia were distributed in the centre of the node with tilt angles in the range $-10^\circ \leq \theta \leq 10^\circ$. A negative tilt angle denotes an anterior tilt and 7/17 cilia were tilted in the anterior direction. The early headfold stage is modelled with 21 cilia with tilt angles in the range $-10^\circ \leq \theta \leq 15^\circ$ with 3/21 cilia tilted in the anterior direction. The late headfold stage is modelled with 25 cilia with tilt angles in the range $-5^\circ \leq \theta \leq 20^\circ$ with only 1/25 cilia tilted in the anterior direction. The 1 somite stage is modelled with 28 cilia with tilt angles in the range $20^\circ \leq \theta \leq 35^\circ$ and the 3 somite stage is modelled with 28 cilia with tilt angles in the range $35^\circ \leq \theta \leq 45^\circ$. Thus we model the increased numbers of cilia and increases in posterior tilt occurring with each advance with developmental stage, consistent with the experimental observations of approximately 150 cilia at the late bud stage and approximately 380 cilia at the 3 somite stage.

3.4 Particle transport

Results presented in this section will adopt the convention of the ‘left’ of the node on the right of the figure, with the following set of scalings: length is normalised with respect to cilium length, which is typically $3\text{--}5\ \mu\text{m}$ for the mouse. Time is scaled with respect to a beat period, $2\pi/\omega$, where ω is the angular frequency and velocities are then scaled according to these length and time scalings.

Figs. 11, 12 and 13 show the results of particle tracking simulations. In these simulations, one beat cycle takes 60 timesteps and the tracking simulations were run for 20,000 timesteps or approximately 333 beat cycles, corresponding to 30 seconds of cilium rotation at 10 Hz. Initial particle positions are shown with an arrow. Particles released in the late bud and early headfold stages of development are swept around the node, in a clockwise vortex when viewed from the ventral side (figs. 11, 12). This is because each cilium has a low tilt angle, thereby generating a local vortex; these local vortices combine to form a larger global vortex.

Particle paths in the late headfold stage vary with position in the node. A particle released in the right of the node at initial height $x_3 = 1.1$ is advected initially to the right and then to the left by neighbouring cilia (fig. 11). A particle with initial height $x_3 = 0.5$ (fig. 12) is advected in a vortical flow around the entire node.

All particles released in the 1 somite and 3 somite stages are advected leftward by a succession of cilia (figs. 11, 12). Once the paths reach the edge of the cilia array at the left of the node they return via a rightward path close to the covering membrane. A leftward particle path is observed because all cilia are tilted towards the posterior at the 1 somite stage of development. The behaviour of particles released above the cilia tips in the left region of the node is shown in fig. 13. At all stages of development the particle path shows the expected return flow characteristics of each stage.

The change from a global vortex to a directional flow effectively breaks the symmetry of the left-right axis. This is because particles may be moved towards the left by a succession of posteriorly tilted cilia as opposed to being carried in a global vortex around the node by untilted cilia. The mechanism for how this flow is converted to asymmetric gene expression is still under active investigation.

4 Swimming in non-Newtonian fluids

For a wide class of problems, for instance internal fertilisation in mammals, the Stokes flow equations do not give an accurate representation of the fluid environment. In such

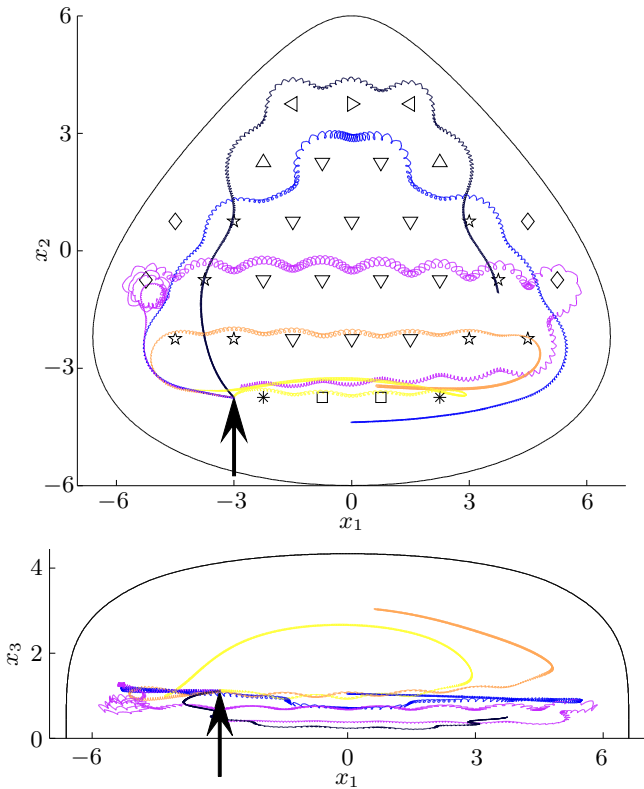


Figure 11: Particle paths for the late bud (—), early headfold (—), late headfold (—), 1 somite (—) and 3 somite (—) stages of development. Note that the right hand side of the figure (positive x_1) corresponds to the eventual ‘left’ axis of the embryo. Cilia positions are denoted by ∇ , \triangleleft , \triangleright , \triangle , \star , \diamond , \square , $*$, where ∇ are present at all stages, \triangleleft , late bud only, \triangleright , late bud, early headfold, late headfold only, \triangle , late bud, 1 somite only, \star , early headfold, late headfold, 1 somite, 3 somite only, \diamond , late headfold, 1 somite, 3 somite only, \square , 1 somite, 3 somite only, $*$, 3 somite only. The initial position for each trajectory is marked with an arrow at $x_1 = -3.00$, $x_2 = -3.75$, $x_3 = 1.10$, showing the x_1x_2 projection in the upper panel and the x_1x_3 projection in the lower panel.

cases, complex fluid rheological properties can have a significant impact upon swimming speed [13], and the need for detailed study of non-Newtonian swimming has long been recognised [47, 48]. Whilst much insight has been gained into the effects of viscoelastic rheology [19, 49, 50], relatively less study has been given to understanding the impact of shear-dependent viscosity on viscous swimming.

We will model swimming in generalised Newtonian flu-

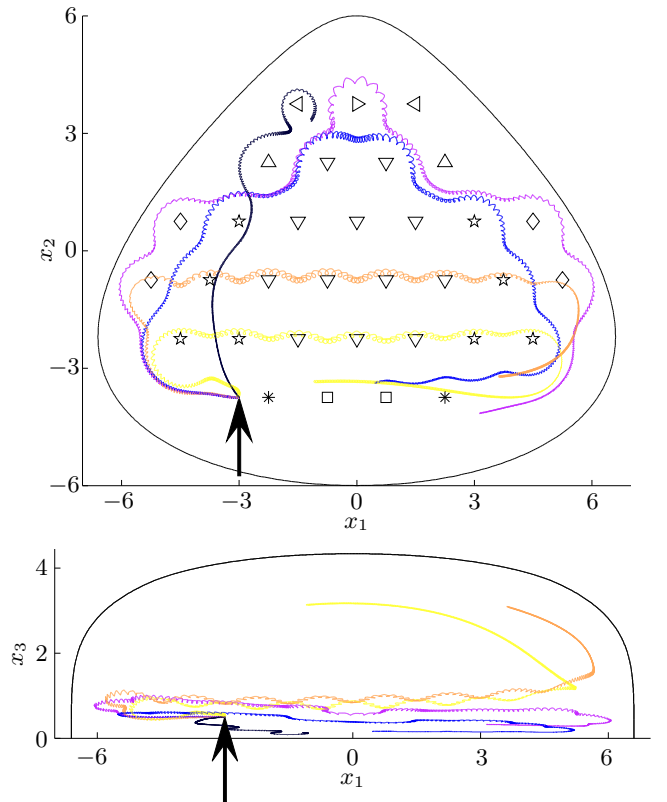


Figure 12: Particle paths for the late bud, early headfold, late headfold, 1 somite and 3 somite stages of development. Cilia positions are denoted as in fig. 11. The initial position for each trajectory is marked with an arrow at $x_1 = -3.00$, $x_2 = -3.75$, $x_3 = 0.50$, showing the x_1x_2 projection in the upper panel and the x_1x_3 projection in the lower panel.

ids for which the effective fluid viscosity, μ_{eff} , is a function of $\dot{\gamma} = (\frac{1}{2}\varepsilon_{ij}(\mathbf{u})\varepsilon_{ij}(\mathbf{u}))^{1/2}$, the second invariant of the strain rate tensor $\varepsilon_{ij} = (\partial_j u_i + \partial_i u_j)$. The governing equations for such fluids are given by

$$\nabla \cdot (\mu_{\text{eff}}(\dot{\gamma})\varepsilon(\mathbf{u})) - \nabla p + \mathbf{F} = 0, \quad (17a)$$

$$\nabla \cdot \mathbf{u} = 0, \quad (17b)$$

which are typically nonlinear, and thus established techniques involving the superposition of fundamental flow solutions are not appropriate.

4.1 Swimming in shear-thinning rheology

Long polymer chains in suspension tend to untangle and align with the flow. Such suspensions are said to be

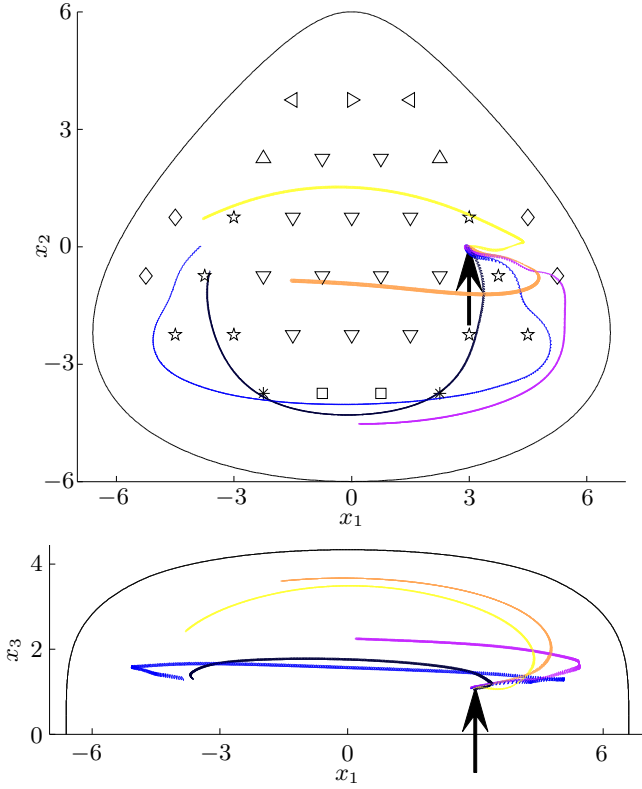


Figure 13: As fig. 12, with initial particle position at $x_1 = 3.00$, $x_2 = 0.00$, $x_3 = 1.10$.

‘shear-thinning’, since their effective viscosity decreases with fluid shear. A swimmer in shear-thinning fluid creates an envelope of thinned fluid around itself, which has a non-trivial effect on its locomotion [13].

The dynamics of polymer suspensions, such as cervical mucus, may be modelled by eq. (17) with the Carreau constitutive law [51], for which

$$\mu_{\text{eff}}(\dot{\gamma}) = \mu_{\infty} + (\mu_0 - \mu_{\infty})(1 + (\lambda\dot{\gamma})^2)^{(n-1)/2}. \quad (18)$$

For Carreau fluids, the effective viscosity decreases monotonically between a zero strain rate viscosity, μ_0 , and an infinite strain rate viscosity μ_{∞} . The material constant λ is a measure of the polymer chain relaxation time.

Using the scalings $\mathbf{u} = \omega L \hat{\mathbf{u}}$, $\mathbf{x} = L \hat{\mathbf{x}}$, $t = 2\pi t/\omega$, $\mathbf{f} = \mu_{\infty} \omega L \hat{\mathbf{f}}$ and $p = \mu_{\infty} \omega \hat{p}$, where ω is the angular beat frequency and L is a characteristic length, for instance the length of the flagellum, the dimensionless momentum

equation governing the Carreau fluid is

$$\hat{\nabla} \cdot \left[\left(1 + \left[\frac{\mu_0}{\mu_{\infty}} - 1 \right] \left[1 + (\lambda \omega \hat{\gamma})^2 \right]^{(n-1)/2} \right) \hat{\boldsymbol{\varepsilon}}(\hat{\mathbf{u}}) \right] - \hat{\nabla} \hat{p} + \hat{\mathbf{F}} = 0. \quad (19)$$

For fixed beat kinematics, the trajectory is thus dependent upon three dimensionless quantities: the ratio μ_0/μ_{∞} of the zero to infinite shear rate viscosities, the product $\lambda\omega$ of the characteristic relaxation time of the fluid with the angular beat frequency, known as the Deborah number De , and the power-law index n .

4.2 Modelling non-Newtonian swimming with femlets

We use the method of femlets, described in Montenegro-Johnson *et al.* [13], to model viscous swimming in a generalised Newtonian fluid. The method of regularised Stokeslets and the method of femlets represent the interaction of the swimmer with the fluid through a set of concentrated ‘blob’ forces of unknown strength and direction. While the method of regularised Stokeslets reduces the problem to finding the coefficients in a linear superposition of velocity solutions of known form, the method of femlets proceeds by applying the finite element method to solve simultaneously the fluid velocity field and the strength and direction of the forces. The use of the finite element method removes the need for the governing equations to be linear. Henceforth, we will continue to use dimensionless variables, but doff hats for conciseness.

Let D be a bounded domain in \mathbb{R}^d , where in our case $d = 2$. We partition the domain boundary $\partial D = \partial D_{\text{dir}} \cup \partial D_{\text{neu}}$ into those portions on which Dirichlet and Neumann type boundary conditions are applied respectively. The surface of the swimmer, $\partial D_{\text{swim}} \subset \partial D_{\text{dir}}$ forms a part of the Dirichlet boundary. However, we will model the interaction of ∂D_{swim} with the fluid by an immersed body force distribution. Thus for our case ∂D_{swim} is not a domain boundary, but rather a manifold containing points within the domain.

Let $H^1(D)$ be the standard Sobolev space of weakly differentiable functions [52] defined on D , and

$$V_E = \left\{ \mathbf{w} \in (H^1(D))^d : \mathbf{w}|_{\partial D_{\text{dir}}} = \mathbf{u}_{\text{dir}} \right\}, \quad (20a)$$

$$V_0 = \left\{ \mathbf{w} \in (H^1(D))^d : \mathbf{w}|_{\partial D_{\text{dir}}} = \mathbf{0} \right\}, \quad (20b)$$

where \mathbf{u}_{dir} are the Dirichlet conditions imposed on ∂D_{dir} . Let also $Q = L^2(D)$. Multiplying (17a), (17b) by arbitrary ‘test’ functions $\mathbf{v} \in V_0$, $q \in Q$, respectively, yields the following integral form of problem (17):

$$\int_D \{ \nabla \cdot [\mu_{\text{eff}}(\dot{\gamma}) \boldsymbol{\varepsilon}(\mathbf{u})] - \nabla p + \mathbf{F} \} \cdot \mathbf{v} \, d\mathbf{x} = 0, \quad (21a)$$

$$\int_D q \nabla \cdot \mathbf{u} \, d\mathbf{x} = 0. \quad (21b)$$

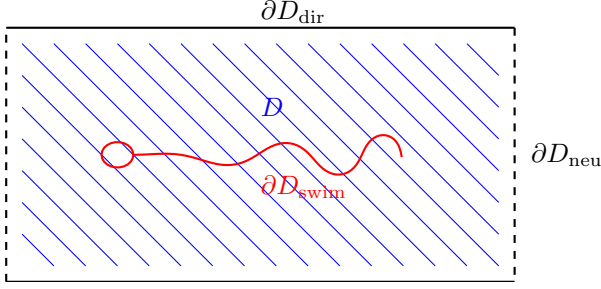


Figure 14: An example domain D containing a model human sperm ∂D_{swim} (red), showing no-slip channel walls ∂D_{dir} (solid, black) and open boundaries ∂D_{neu} (dashed, black).

Integration by parts yields an equivalent integral formulation with reduced differentiability requirements for \mathbf{u} and p . This is known as the weak (or variational) formulation of the generalised Stokes flow problem (17) and reads:

Find $(\mathbf{u}, p) \in V_E \times Q$ such that $\forall (\mathbf{v}, q) \in V_0 \times Q$,

$$\int_D \mu_{\text{eff}}(\dot{\gamma}) \boldsymbol{\varepsilon}(\mathbf{u}) : \boldsymbol{\varepsilon}(\mathbf{v}) \, d\mathbf{x} - \int_D p \nabla \cdot \mathbf{v} \, d\mathbf{x} + \int_D \mathbf{F} \cdot \mathbf{v} \, d\mathbf{x} = 0, \quad (22a)$$

$$\int_D q \nabla \cdot \mathbf{u} \, d\mathbf{x} = 0, \quad (22b)$$

so that V_E, V_0 are the velocity solution and test function spaces respectively. Applied on ∂D_{neu} is the open boundary condition first proposed by Papanastasiou *et al.* [53], given in our case by

$$\int_{\partial D_{\text{neu}}} \mathbf{v} \cdot \boldsymbol{\sigma} \cdot \mathbf{n} \, d\mathbf{x} = 0. \quad (23)$$

Existence and uniqueness for problem (22) was shown by Baranger *et al.* [54] for both the power law and Carreau models. The finite element discretisation used herein is discussed by Barrett *et al.* [55].

We consider swimmers in truncated channels of the form shown in fig. 14. The no-slip condition $\mathbf{u} = \mathbf{0}$ is applied on the the channel walls ∂D_{dir} , and on the boundaries where the domain has been truncated ∂D_{neu} we apply the open boundary condition (23). The results we will present were obtained in a channel of height 5 and length 11, with lengths normalised to a characteristic length for the swimmer.

As the swimmer moves through the fluid, the moving boundary exerts a force distribution on the fluid that drives the flow. We incorporate this interaction through

the unknown body force \mathbf{F} , which is governed by the motion of the swimmer. We approximate \mathbf{F} by a finite number of smooth immersed forces of unknown strength and direction (femlets)

$$\mathbf{F} = \sum_{k=1}^{N_f} g^\epsilon(\mathbf{x} - \mathbf{x}_k) \mathbf{f}_k, \quad (24)$$

for N_f femlets of strength \mathbf{f}_k , located at \mathbf{x}_k . The cut-off function $g^\epsilon(\mathbf{x} - \mathbf{x}_k)$ is a regularisation function similar to that used in the method of regularised Stokeslets [43]

Associated with each femlet are K degrees of freedom, where K is the dimensionality of the problem domain. For example, a swimmer in two dimensions would have the lab frame force of each femlet in the x and y directions, (f_1, f_2) , as unknowns, resulting in $2 \times N_f$ additional scalar variables.

To calculate the $2 \times N_f$ force unknowns, we enforce $2 \times N_f$ constraints in the form of Dirichlet velocity conditions \mathbf{u}_s . These are given by the swimmer's velocity in the body frame, in which the swimmer neither rotates nor translates, and applied at the location of each femlet. The relationship between the body frame and the lab frame is shown in fig. 15. The body frame velocity \mathbf{u}_b is related to the lab frame velocity \mathbf{u} solved for in problem (22) by

$$\mathbf{u}_b = \mathbf{u} - \mathbf{U} - \boldsymbol{\Omega} \times (\mathbf{x} - \mathbf{x}_0), \quad (25)$$

where $\mathbf{U}, \boldsymbol{\Omega}$ are the translational and angular velocities of the swimmer respectively and \mathbf{x}_0 is a fixed point on the swimmer.

The translational and angular velocities $\mathbf{U}, \boldsymbol{\Omega}$ provide additional unknowns which are closed by the conditions that zero net force and torque act on the swimmer,

$$\sum_{k=1}^{N_f} \mathbf{f}_k \int_D g^\epsilon(\mathbf{x} - \mathbf{x}_k) \, d\mathbf{x} = 0, \quad (26a)$$

$$\sum_{k=1}^{N_f} \mathbf{f}_k \times \mathbf{x}_k \int_D g^\epsilon(\mathbf{x} - \mathbf{x}_k) \, d\mathbf{x} = 0. \quad (26b)$$

All femlets are given the same cut-off function g^ϵ , and the swimming velocity conditions are applied at the function's centroid, \mathbf{x}_k . Thus, the force and torque conditions on the swimmer may be written

$$\sum_{k=1}^{N_f} \mathbf{f}_k = 0, \quad \sum_{k=1}^{N_f} \mathbf{f}_k \times \mathbf{x}_k = 0, \quad (27)$$

respectively. Under these conditions, problem (22) be-

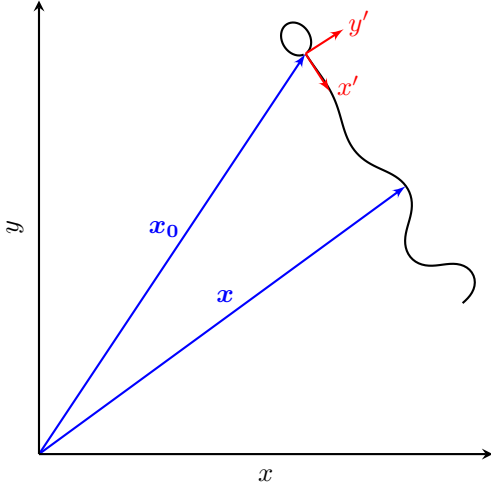


Figure 15: Schematic of the relationship between the lab frame (x, y) and the body frame (x', y') , where \mathbf{x} is a general point on the swimmer, given in the lab frame and \mathbf{x}_0 is a reference point on the swimmer. The transformation from body frame velocity to lab frame velocity is given by eq. (25).

comes

Find $(\mathbf{u}, p) \in V_E \times Q$ such that $\forall (\mathbf{v}, q) \in V_0 \times Q$,

$$\int_D \mu_{\text{eff}}(\dot{\gamma}) \boldsymbol{\varepsilon}(\mathbf{u}) : \boldsymbol{\varepsilon}(\mathbf{v}) \, d\mathbf{x} - \int_D p \nabla \cdot \mathbf{v} \, d\mathbf{x} + \int_D \left[\sum_{k=1}^{N_f} g^\epsilon(\mathbf{x} - \mathbf{x}_k) \mathbf{f}_k \right] \cdot \mathbf{v} \, d\mathbf{x} = 0, \quad (28a)$$

$$\int_D q \nabla \cdot \mathbf{u} \, d\mathbf{x} = 0, \quad (28b)$$

subject to,

$$\mathbf{u}(\mathbf{x}_k, t) = \mathbf{u}_s(\mathbf{x}_k, t) + \mathbf{U}(t) - \boldsymbol{\Omega}(t) \times (\mathbf{x}_k - \mathbf{x}_0), \quad (28c)$$

$$\sum_{k=1}^{N_f} \mathbf{f}_k = 0, \quad \sum_{k=1}^{N_f} \mathbf{f}_k \times \mathbf{x}_k = 0. \quad (28d)$$

Note that problem (28) is nonlinear, due to the dependence of μ_{eff} on \mathbf{u} . We solve this nonlinear system with the following Picard iteration: given an initial guess (\mathbf{u}^0, p^0) ,

For $m = 0, 1, \dots$ solve until convergence:

Find $(\mathbf{u}^{m+1}, p^{m+1}) \in V_E \times Q$ such that

$\forall (\mathbf{v}, q) \in V_0 \times Q$,

$$\int_D \mu_{\text{eff}}(\dot{\gamma}^m) \boldsymbol{\varepsilon}(\mathbf{u}^{m+1}) : \boldsymbol{\varepsilon}(\mathbf{v}) \, d\mathbf{x} - \int_D p^{m+1} \nabla \cdot \mathbf{v} \, d\mathbf{x} + \int_D \left[\sum_{k=1}^{N_f} g^\epsilon(\mathbf{x} - \mathbf{x}_k) \mathbf{f}_k^{m+1} \right] \cdot \mathbf{v} \, d\mathbf{x} = 0 \quad (29a)$$

$$\int_D q \nabla \cdot \mathbf{u}^{m+1} \, d\mathbf{x} = 0, \quad (29b)$$

subject to

$$\mathbf{u}(\mathbf{x}_k, t)^{m+1} = \mathbf{u}_s(\mathbf{x}_k, t) + \mathbf{U}(t)^{m+1} - \boldsymbol{\Omega}(t)^{m+1} \times (\mathbf{x}_k - \mathbf{x}_0), \quad (29c)$$

$$\sum_{k=1}^{N_f} \mathbf{f}_k^{m+1} = 0, \quad \sum_{k=1}^{N_f} \mathbf{f}_k^{m+1} \times \mathbf{x}_k = 0, \quad (29d)$$

End.

At each iteration the system (29) is discretised by Taylor-Hood P2-P1 triangular finite elements [56] over the domain D , and the resultant linear system $\mathbf{M}(\dot{\gamma}^m) \mathbf{z}^{m+1} = \mathbf{r}$ is solved. The iteration continues until $\|\mathbf{M}(\dot{\gamma}^{m+1}) \mathbf{z}^{m+1} - \mathbf{M}(\dot{\gamma}^m) \mathbf{z}^{m+1}\| < \text{tol}$, a small tolerance here set to $\text{tol} = 10^{-9}$, returning a solution vector \mathbf{z} of the nonlinear swimming problem. The solution, \mathbf{z} , comprises the lab frame velocity of the fluid \mathbf{u} , the fluid pressure p , the force distribution along the swimmer \mathbf{f}_k and the swimming translational \mathbf{U} and rotational $\boldsymbol{\Omega}$ velocities.

4.3 A Najafi-Golestani swimmer in a shear-thinning fluid

Perhaps the simplest conceptual model of a viscous swimmer was proposed by Najafi and Golestani [14]; it is highly instructive to compare the physics of this swimmer to more detailed models of cells equipped with cilia and flagella. The Najafi-Golestani swimmer comprises two outer spheres which move relative to a central sphere with a non-reciprocal motion.

The mechanism underlying the original Najafi-Golestani swimmer is as follows: one of the outer spheres will move at any given time. By force balance, leftward relative motion of an outer sphere results in rightward motion of the remaining spheres through the fluid, and vice versa. The distance that the remaining spheres move in the fluid depends on the drag of the remaining two spheres. Relative leftward motion of an outer sphere occurs while the other spheres are far apart; relative rightward motion of an outer sphere occurs while the other spheres are close together. Hydrodynamic interaction re-

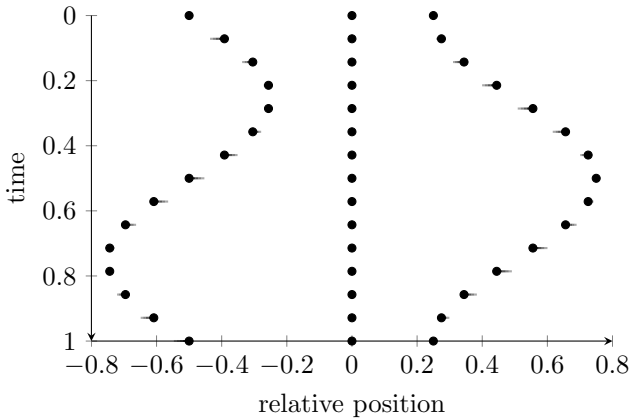


Figure 16: The position of the two outer swimming spheres, modelled by femlets moving relative to the central sphere for $\chi = 1/4$ over the course of a beat cycle.

sults in the drag of the other spheres being reduced when they are close together. Therefore the drag of the remaining spheres is less during relative rightward motion of the active sphere, and so the beat cycle is slightly more effective in moving the swimmer to the left than the right. Our variant of this swimmer follows the suggestion in the original paper of Najafi & Golestanian [14] of making the sphere motion smooth in time.

We model this swimmer by three collinear femlets. The outer femlets move as harmonic oscillators relative to the central femlet, and symmetry is broken by enforcing a phase difference, χ , between them

$$x_1 = -d + \sin(t), \quad x_2 = 0, \quad x_3 = d + \sin(t - \chi), \quad (30)$$

where d is a constant displacement. The locus of this motion is shown over a beat-cycle in fig. 16. Due to the symmetry of the problem domain and beat pattern in the line $y = 0$, the swimmer will move in the x -direction. Fig. 17 shows the progress of this swimmer in Stokes flow for $\chi = 1/4$, so that our example swims in the negative x -direction. Here we normalise length scales such that $2d = 1$. We will now examine the effects of beat phase, as well as the Carreau rheological parameters, on swimming speed.

For the set of rheological parameters: viscosity ratio $\mu_0/\mu_\infty = 2$, Deborah number $\lambda\omega = 1$, and power-law index $n = 1/2$, we first examine the effect of changing the phase difference χ . Fig. 18 shows the progress of the swimmer as a function of χ , revealing a maximum when $\chi = 1/4$ for both Carreau and Stokes flow. This phase difference corresponds to a continuous analogue of the beat pattern

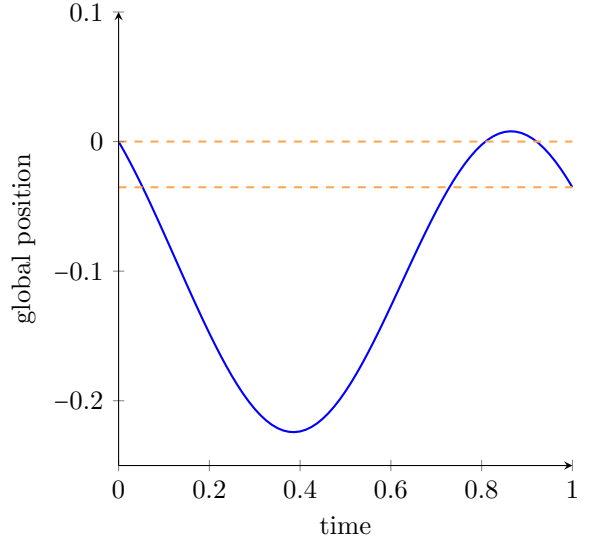


Figure 17: The position of the central sphere of the Najafi-Golestanian swimmer in a channel of Stokes fluid over a beat cycle for $\chi = 1/4$.

proposed in ref. [14]. It should be noted that for fluids with viscoelastic properties, this may not be the optimum phase difference, due to the dependence of the fluid stress on its deformation history. For this set of fluid parameters, the mean benefit to progress is 3%, with a standard deviation of 0.5%. The zero progress solutions at $\chi = 0, 1/2$ correspond to the cases where the swimming spheres are in phase and antiphase respectively. Since the maximum progress is achieved for $\chi = 1/4$, we fix this variable for the remainder of the study.

We now wish to examine the effects of decreasing the power-law index, n . For $n = 1$, the Carreau equations reduce to the Stokes flow equations. Decreasing n leads to a sharper decrease in the effective viscosity for lower strain rates. For $\lambda\omega = 1$ and $\mu_0/\mu_\infty = 2$, progress of the swimmer over a beat-cycle as a function of n is displayed in fig. 19, showing that as n decreases, magnitude of progress per beat increases.

By fixing $\lambda\omega = 1$ and $n = 1/2$, we examine the effects of varying the viscosity ratio μ_0/μ_∞ . Fig. 20 displays the progress of the swimmer over a beat-cycle as a function of this ratio, which shows that as the infinite shear rate viscosity decreases, magnitude of progress increases.

Finally, we consider the effect of altering the Deborah number $De = \lambda\omega$. This is especially important, since for a given fluid, the power-law index and viscosity ratio are fixed physical parameters. However, De is a function of beat frequency, which for artificial swimmers may be con-

trolled and therefore optimised, much like the phase difference χ . For $\mu_0/\mu_\infty = 2$, and $n = 1$, progress over a beat-cycle is displayed as a function of De in fig. 21, which shows that for this particular model swimmer, optimum progress is achieved for $\lambda\omega \approx 0.8$, so that the angular frequency of the swimmer is approximately 4/5 of the characteristic relaxation time of the fluid.

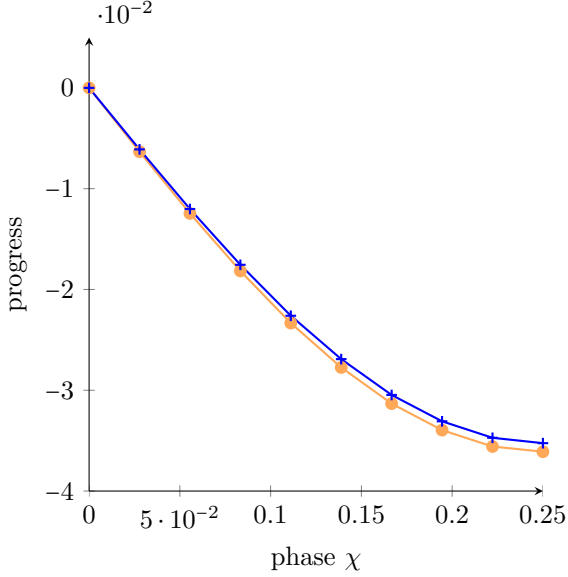


Figure 18: The progress of the Najafi-Golestanian swimmer over a single beat cycle as a function of the phase difference, χ , for Newtonian (blue,+) and Carreau fluid (orange,•) with $\mu_0/\mu_\infty = 2$, $\lambda\omega = 1$ and $n = 1/2$. Negative progress denotes swimming in the negative x -direction.

4.4 A two-dimensional sperm in shear-thinning and thickening fluid

For sperm in high-viscosity fluids, such as human mucus, swimming is typified by planar flagella beating that grows in peak curvature towards the distal portion of the tail [57]. To model this waveform, we prescribe a body-frame tangent angle of the form

$$\psi(s, t) = Cs \cos(ks - t), \quad (31)$$

for s the arclength along the flagellum and t time. Such a parameterisation makes sense in the context of considering a bending wave propagating down the flagellum, steepening towards the distal end as the stiffness of the flagellum decreases. A representative waveform produced by the shear angle parametrisation given by eq. (31) is shown in fig. 22.

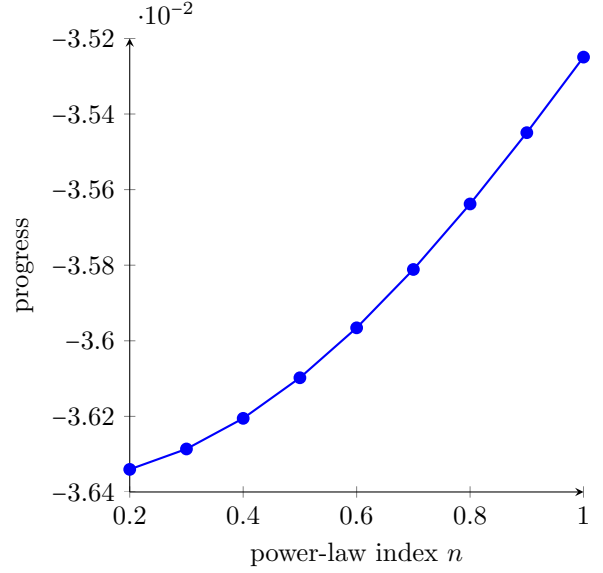


Figure 19: The progress of the Najafi-Golestanian swimmer over a single beat cycle in Carreau fluid as a function of the power-law index, n , for $\lambda\omega = 1$ and $\mu_0/\mu_\infty = 2$. Newtonian flow corresponds to the value $n = 1$. Negative progress denotes swimming in the negative x -direction.

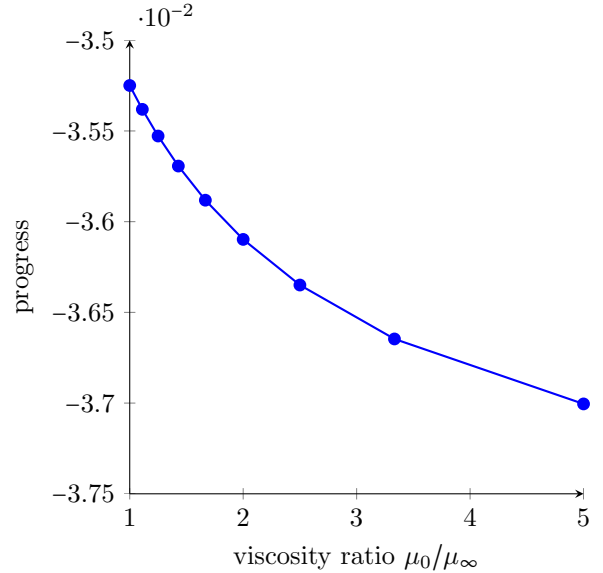


Figure 20: The progress of the Najafi-Golestanian swimmer over a single beat cycle in Carreau fluid as a function of the viscosity ratio, μ_0/μ_∞ , for $\lambda\omega = 1$ and $n = 1/2$, shown for equispaced values of μ_∞ . Newtonian flow corresponds to the value $\mu_0/\mu_\infty = 1$. Negative progress denotes swimming in the negative x -direction.

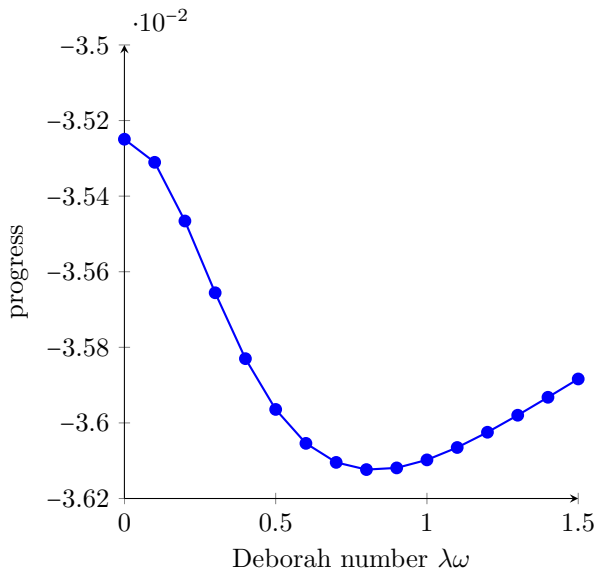


Figure 21: The progress of the Najafi-Golestani swimmer over a single beat cycle in Carreau fluid as a function of the Deborah number, $\lambda\omega$, for $\mu_0/\mu_\infty = 2$ and $n = 1/2$. Newtonian flow corresponds to the value $\lambda\omega = 0$. Negative progress denotes swimming in the negative x -direction.

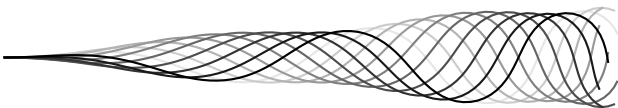


Figure 22: A model flagella waveform, generated by the shear angle parameterisation (31) with amplitude $C = 0.9\pi/2$ and wavenumber $k = 2.5\pi$, typical of what is observed experimentally in high viscosity media.

Integrating the tangent vector along the flagellum gives the flagellar centreline

$$x_c(s, t) = x_0 + \int_0^s \cos(\psi(s', t)) ds', \quad (32a)$$

$$y_c(s, t) = y_0 + \int_0^s \sin(\psi(s', t)) ds', \quad (32b)$$

with corresponding centreline velocity $\dot{\mathbf{x}}$

$$\dot{x}_c(s, t) = \int_0^s -\sin(\psi) \dot{\psi} ds', \quad (33a)$$

$$\dot{y}_c(s, t) = \int_0^s \cos(\psi) \dot{\psi} ds'. \quad (33b)$$

This parameterisation of the flagellum is given in the body frame [58], in which the cell body neither rotates nor translates. The translational and rotational velocities that arise from this instantaneous configuration are then used to update the position of the swimmer in the lab frame, so that the cell swims through the fluid domain.

The trajectory of the swimmer is calculated by integrating the swimming velocity $\mathbf{U}, \mathbf{\Omega}$ with the Adams-Bashforth multistep method [59, 60], which interpolates an n th order polynomial through the current and previous $n-1$ values of translational and angular velocity to give the position. For a two-dimensional sperm-like swimmer in a channel of Newtonian fluid, with less than a 0.3% change in the position of the swimmer after a single beat cycle between 25 steps per beat with the second order scheme and 80 steps with the third order scheme. As such, we use the second order scheme with 25 steps per beat. We normalise length scales to the flagellum length, so that one length unit corresponds to $55 \mu\text{m}$, and time scales to the period of the beat. Thus, modelling a tail beating at 10 Hz would mean that one time unit corresponds to $1/10\text{s}$.

Fig. 23 shows the sperm's progress as a function of Deborah number for $\mu_0/\mu_\infty = 2$ and $n = 1/2$. Note the qualitative similarity to fig. 21, with overall progression initially increasing with De to a maximum value around $De = 0.8$, then decreasing at a slower rate. Since the Najafi-Golestani swimmer comprises three forces in balance, its representation by a Stokes quadrupole might shed insight into this link, motivated by the observations in fig. 6. These results also draw an interesting parallel with the analysis of Teran *et al.* [50] who used the immersed boundary method to show that the progression of a waving filament may be enhanced in a viscoelastic Oldroyd B fluid at Deborah numbers close to 1.

If the viscosity ratio, μ_0/μ_∞ , is less than 1, then the effective viscosity (18) of a Carreau fluid increases with shear rate. For such a model, the relaxation time λ no longer has a physical interpretation in terms of polymer

physics, but the Carreau law may still be used as a regularisation of a shear-thickening power-law fluid. Examples of shear-thickening fluids are custard and a mixture of cornstarch with water known colloquially as oobleck.

Fig. 24 shows the progress of the sperm over a single beat-cycle as a function of the viscosity ratio μ_0/μ_∞ . Stokes flow, corresponding to $\mu_0/\mu_\infty = 1$, is marked in orange, and the thickening and thinning régimes lie to its left and right respectively. We see that whilst shear-thinning aids progress, shear-thickening inhibits it. Furthermore, fig. 24 shows an almost perfect linear relationship between progress and the logarithm of μ_0/μ_∞ .

For shear-thinning fluids, there is a gradient of thick to thin fluid from the proximal to distal portions of the flagellum. For shear-thickening fluids, the gradient runs from thin to thick. Thus, the disadvantage to cell progress in a shear-thickening fluid is consistent with the hypothesis of Montenegro-Johnson *et al.* [13] that differential viscosity between the distal and proximal portions of the flagellum is responsible for changes in propulsive efficiency.

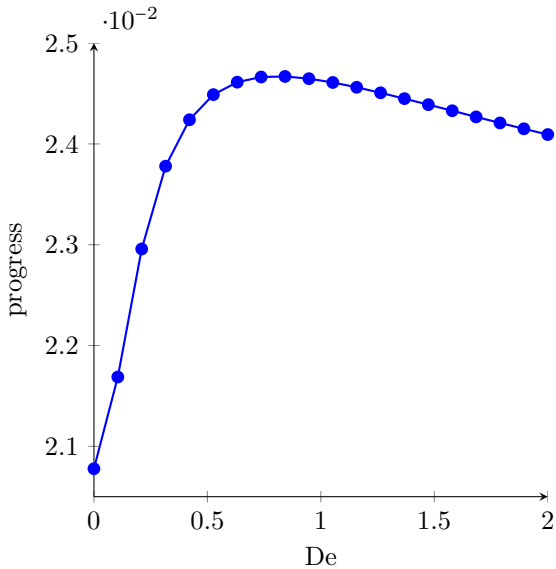


Figure 23: The unsigned total distance travelled by our two-dimensional sperm over a single beat cycle in Carreau fluid as a function of the Deborah number, $\lambda\omega$, for $\mu_0/\mu_\infty = 2$ and $n = 1/2$. Newtonian flow corresponds to the value $\lambda\omega = 0$.

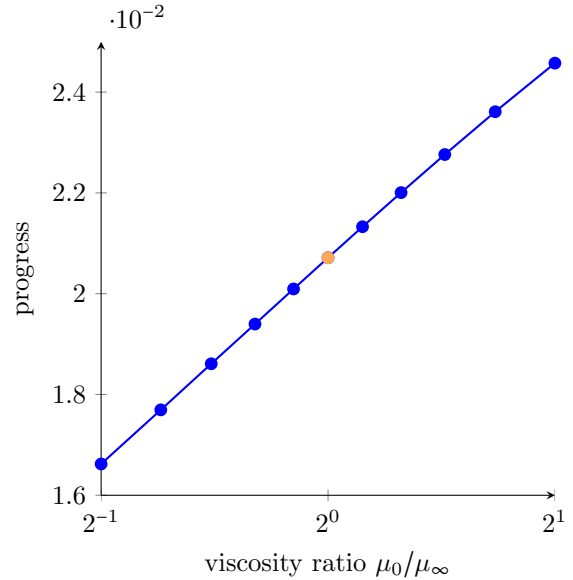


Figure 24: The progress of the two-dimensional sperm-like swimmer over a single beat cycle in Carreau fluid as a function of the viscosity ratio, μ_0/μ_∞ , for $\lambda\omega = 1$ and $n = 1/2$. Stokes flow, $\mu_0/\mu_\infty = 1$ is marked in orange, with the shear-thickening régime for $\mu_0/\mu_\infty < 1$ and the shear-thinning régime for $\mu_0/\mu_\infty > 1$. The horizontal axis is displayed on a logarithmic scale μ_0/μ_∞ .

5 Conclusions

5.1 Fundamental physics of cilia and flagella driven flow

The linearity of the Stokes flow equations makes the method of singular solutions possible. This approach provides significant insight into the basic nature of the physics of propulsion and swimming. Microscopic swimmers, for which gravitational and inertial forces are negligible, are subject to zero total force and torque, entailing that the far-field of a flagellated swimmer is stresslet in nature, the flow velocity having inverse square decay. However, within a distance of a few cell radii or flagella lengths, the flow field can be markedly different from a stresslet, being closer to a Stokes quadrupole for sperm, and a stresslet-source dipole combination for single celled algae. These findings are confirmed both experimentally and through more detailed computational models. The action of gravity on larger swimmers results in a more slowly-decaying $\mathcal{O}(1/r)$ Stokeslet flow.

The lack of explicit time dependence in the Stokes flow equations entails that time-irreversible motion is essential for successful swimming and pumping. Cilia and flagella achieve this through a number of mechanisms. The anisotropy of the Stokeslet results in the anisotropic drag law for slender bodies, a property which underlies the propulsive effect of travelling bending waves. Finally, wall interaction, which can be understood by the method of images, is essential to the function of cilia. Image systems convert both forces and torques to higher order singularities in the far-field, a mechanism which explains how rotating embryonic nodal cilia create a right-to-left flow.

5.2 Cilia in embryonic development

The hybrid computational technique combining slender body theory with the regularised Stokeslet boundary element method allows prediction of both generic features of cilia-driven flow in the nodal cavity, as shown previously [28]. Our simulations show the effect of developmental changes in cilia orientation and position, using experimental data on cilia numbers and orientation [38]. In early stages of development (late bud, early headfold), the flow is essentially vortical, whereas in later stages when the majority of cilia are tilted posteriorly (late headfold, 1 somite and 3 somite); an asymmetric directional flow is established that breaks the symmetry of the left-right axis.

Qualitative agreement with particle imaging velocimetry observations [38] suggest that this approach will be useful for analysing this and related systems in more detail, providing further physical insight into the coupling

of nodal flow to subsequent morphogenesis [32, 61].

5.3 Swimming in non-Newtonian fluids

The Najafi-Golestanian swimmer is able to progress because of hydrodynamic interaction of spheres coupled with time-irreversible motion, whereas sperm propel through propagating bending waves of a slender flagellum; however the effect of shear-thinning rheology on both cells is qualitatively similar. Both models swim faster in a shear-thinning fluid, with an optimal value for Deborah number between 0.5 and 1, however sperm enjoy a greater propulsive advantage relative to the Newtonian state compared with the three-sphere swimmer, their increase being up to around 20% compared with around 3% in the region of parameter space investigated. For sperm, shear-thickening fluid rheology led to a decrease in cell progress. It was found that cell progress had an almost exact logarithmic dependence on the viscosity ratio μ_0/μ_∞ . It should be noted, however, that the fluid strain-rate of a Carreau fluid is independent of its recent deformation history, and so to fully capture the behaviour of human mucus an extended model is desirable.

5.4 Summary

The examples in this paper illustrate aspects of the broad range of very low Reynolds number flow. The embryonic nodal flow is typically considered Newtonian, and entails the wall effect converting rotation to directional flow, which in turn converts chiral to lateral information. The swimming cell problems illustrate the importance of more complex non-Newtonian effects typical of biological fluids such as blood and mucus, and the qualitative insights that can be gained from conceptual models.

Reproduction and development continue to be inspirational topics in the biological fluid mechanics of active matter. Future work will focus on, among other topics, the nonlinear interaction of multiple ciliated and flagellated cells with biological fluids and with each other. We anticipate that the techniques described will help to form a basis for these future investigations.

Acknowledgements

TDMJ and AAS acknowledge Engineering and Physical Sciences Research Council PhD studentships. DJS is funded by a Birmingham Science City Research Alliance Fellowship. Computations in sect. 3 were performed using the University of Birmingham BlueBEAR HPC service, which was purchased through HEFCE SRIF-3 funds.

References

- [1] G. I. Taylor. Analysis of the swimming of microscopic organisms. *Proc. R. Soc. Lond. A*, pages 447–461, 1951.
- [2] W. Engelmann. *Über die flimmerbewegung*. Engelmann, 1868.
- [3] M. Verworn. Studien zur physiologie der flimmerbewegung. *Pflugers Arch.*, 48(1):149–180, 1891.
- [4] G. H. Parker. The movements of the swimming-plates in ctenophores, with reference to the theories of ciliary metachronism. *J. Exp. Zool.*, 2(3):407–423, 1905.
- [5] J. Gray. *Ciliary movement*. Cambridge Comparative Physiology. Cambridge Univ. Pr., 1928.
- [6] G. J. Hancock. The self-propulsion of microscopic organisms through liquids. *Proc. R. Soc. Lond. A*, 217(1128):96–121, 1953.
- [7] S. Nonaka, Y. Tanaka, Y. Okada, S. Takeda, A. Harada, Y. Kanai, M. Kido, and N. Hirokawa. Randomization of left-right asymmetry due to loss of nodal cilia generating leftward flow of extraembryonic fluid in mice lacking KIF3B motor protein. *Cell*, 95(6):829–837, 1998.
- [8] I. Manton and B. Clarke. An electron microscope study of the spermatozoid of sphagnum. *J. Exp. Biol.*, 3(3):265–275, 1952.
- [9] D. W. Fawcett. The study of epithelial cilia and sperm flagella with the electron microscope. *The Laryngoscope*, 64(7):557–567, 1954.
- [10] B. Afzelius. Electron microscopy of the sperm tail results obtained with a new fixative. *J. Biophys. Biochem. Cytol.*, 5(2):269–278, 1959.
- [11] P. Satir. Studies on cilia: II. examination of the distal region of the ciliary shaft and the role of the filaments in motility. *J. Cell Biol.*, 26(3):805–834, 1965.
- [12] E. M. Purcell. Life at low Reynolds number. *Amer. J. Phys.*, 45(1):3–11, 1977.
- [13] T. Montenegro-Johnson, D. J. Smith, and D. Loghin. Modelling microscopic swimming in shear-thinning fluids. *Submitted*, 2012.
- [14] A. Najafi and R. Golestanian. Simple swimmer at low Reynolds number: three linked spheres. *Phys. Rev. E*, 69:062901, 2004.
- [15] D. W. Fawcett. The mammalian spermatozoon. *Dev. Biol.*, 44(2):394–436, 1975.
- [16] N. Hirokawa, Y. Tanaka, Y. Okada, and S. Takeda. Nodal flow and the generation of left-right asymmetry. *Cell*, 125(1):33–45, 2006.
- [17] S. Nonaka, S. Yoshida, D. Watanabe, S. Ikeuchi, T. Goto, W. F. Marshall, and H. Hamada. De novo formation of left-right asymmetry by posterior tilt of nodal cilia. *PLoS Biol.*, 3(8):1467–1472, 2005.
- [18] J. Gray and G. J. Hancock. The propulsion of sea-urchin spermatozoa. *J. Exp. Biol.*, 32(4):802–814, 1955.
- [19] O. S. Pak and E. Lauga. Extensibility enables locomotion under isotropic drag. *Phys. Fluids*, 23:081702, 2011.
- [20] J. R. Blake and M. A. Sleight. Mechanics of ciliary locomotion. *Biol. Rev. Camb. Phil. Soc.*, 49(1):85–125, 1974.
- [21] A. T. Chwang and T. Y. Wu. A note on the helical movement of micro-organisms. *Proc. R. Soc. Lond. B*, 178(1052):327–346, 1971.
- [22] J. R. Blake. A note on the image system for a Stokeslet in a no-slip boundary. *Proc. Camb. Phil. Soc.*, 70:303–310, 1971.
- [23] A. Vilfan and F. Jülicher. Hydrodynamic flow patterns and synchronization of beating cilia. *Phys. Rev. Lett.*, 96(5):58102, 2006.
- [24] K. Drescher, R. E. Goldstein, N. Michel, M. Polin, and I. Tuval. Direct measurement of the flow field around swimming microorganisms. *Phys. Rev. Lett.*, 105(16):168101, 2010.
- [25] K. Drescher, J. Dunkel, L. H. Cisneros, S. Ganguly, and R. E. Goldstein. Fluid dynamics and noise in bacterial cell-cell and cell-surface scattering. *Proc. Natl. Acad. Sci. USA*, 108(27):10940–10945, 2011.
- [26] D. J. Smith and J. R. Blake. Surface accumulation of spermatozoa: A fluid dynamic phenomenon. *The Mathematical Scientist*, 34(2):74–87, 2009.
- [27] D. J. Smith, E. A. Gaffney, and J. R. Blake. Discrete cilia modelling with singularity distributions: application to the embryonic node and the airway surface liquid. *B. Math. Biol.*, 69(5):1477–1510, 2007.

- [28] D. J. Smith, A. A. Smith, and J. R. Blake. Mathematical embryology: the fluid mechanics of nodal cilia. *J. Eng. Math.*, 70(1):255–279, 2011.
- [29] R. H. Dillon, L. J. Fauci, C. Omoto, and X. Yang. Fluid dynamic models of flagellar and ciliary beating. *Ann. New York Acad. Sci.*, 1101(1):494–505, 2007.
- [30] E. Lauga and T. R. Powers. The hydrodynamics of swimming microorganisms. *Rep. Prog. Phys.*, 72:096601, 2009.
- [31] E. A. Gaffney, H. Gadêlha, D. J. Smith, J. R. Blake, and J. C. Kirkman-Brown. Mammalian sperm motility: observation and theory. *Annu. Rev. Fluid Mech.*, 43:501–528, 2011.
- [32] N. Hirokawa, Y. Okada, and Y. Tanaka. Fluid dynamic mechanism responsible for breaking the left-right symmetry of the human body: The nodal flow. *Annu. Rev. Fluid Mech.*, 41:53–72, 2009.
- [33] W. E. Berdon, C. McManus, and B. Afzelius. More on Kartagener’s syndrome and the contributions of Afzelius and A.K. Siewert. *Pediat. Radiol.*, 34(7):585–586, 2004.
- [34] A. Hilfinger and F. Jülicher. The chirality of ciliary beats. *Phys. Bio.*, 5:016003, 2008.
- [35] J. H. E. Cartwright, O. Piro, and I. Tuval. Fluid-dynamical basis of the embryonic development of left-right asymmetry in vertebrates. *Proc. Natl. Acad. Sci. USA*, 101(19):7234–7239, 2004.
- [36] C. J. Brokaw. Computer simulation of flagellar movement IX. Oscillation and symmetry breaking in a model for short flagella and nodal cilia. *Cell Motil. Cytoskel.*, 60(1):35–47, 2005.
- [37] D. J. Smith, J. R. Blake, and E. A. Gaffney. Fluid mechanics of nodal flow due to embryonic primary cilia. *J. R. Soc. Interface*, 5(22):567–573, 2008.
- [38] M. Hashimoto, K. Shinohara, J. Wang, S. Ikeuchi, S. Yoshida, C. Meno, S. Nonaka, S. Takada, K. Hatta, A. Wynshaw-Boris, and H. Hamada. Planar polarization of node cells determines the rotational axis of node cilia. *Nat. Cell Biol.*, 12(2):170–176, 2010.
- [39] K. M. Downs and T. Davies. Staging of gastrulating mouse embryos by morphological landmarks in the dissecting microscope. *Development*, 118(4):1255, 1993.
- [40] R. E. Johnson. An improved slender-body theory for Stokes flow. *J. Fluid Mech.*, 99(2):411–431, 1980.
- [41] J. R. Blake and A. T. Chwang. Fundamental singularities of viscous flow. *J. Eng. Math.*, 8(1):23–29, 1974.
- [42] A. T. Chwang and T. Y. Wu. Hydromechanics of low-Reynolds-number flow. Part 2. Singularity method for Stokes flows. *J. Fluid Mech.*, 67(4):787–815, 1975.
- [43] R. Cortez. The method of regularized Stokeslets. *SIAM J. Sci. Comput.*, 23(4):1204–1225, 2001.
- [44] R. Cortez, L. Fauci, and A. Medovikov. The method of regularized Stokeslets in three dimensions: analysis, validation, and application to helical swimming. *Phys. Fluids*, 17(031504):1–14, 2005.
- [45] J. Ainley, S. Durkin, R. Embid, P. Boindala, and R. Cortez. The method of images for regularized Stokeslets. *J. Comp. Phys.*, 227(9):4600–4616, 2008.
- [46] D. J. Smith. A boundary element regularized Stokeslet method applied to cilia- and flagella-driven flow. *Proc. R. Soc. Lond. A*, 465:3605–3626, 2009.
- [47] R. N. Mills and D. F. Katz. A flat capillary tube system for assessment of sperm movement in cervical mucus. *Fertil. Steril.*, 29(1):43–47, 1978.
- [48] D. F. Katz, J. W. Overstreet, and F. W. Hanson. A new quantitative test for sperm penetration into cervical mucus. *Fertil. Steril.*, 33(2):179–186, 1980.
- [49] H. C. Fu, C. W. Wolgemuth, and T. R. Powers. Swimming speeds of filaments in nonlinearly viscoelastic fluids. *Phys. Fluids*, 21:033102, 2009.
- [50] J. Teran, L. Fauci, and M. Shelley. Viscoelastic fluid response can increase the speed and efficiency of a free swimmer. *Phys. Rev. Lett.*, 104(3):38101, 2010.
- [51] P. J. Carreau. *Rheological equations from molecular network theories*. University of Wisconsin-Madison, 1968.
- [52] D. Braess. *Finite elements: theory, fast solvers, and applications in solid mechanics*. Cambridge Univ. Pr., 2007.
- [53] T.C. Papanastasiou, N. Malamataris, and K. Ellwood. A new outflow boundary condition. *Int. J. Numer. Meth. Fluids*, 14(5):587–608, 1992.

- [54] J. Baranger and K. Najib. Analyse numérique des écoulements quasi-newtoniens dont la viscosité obéit à la loi puissance ou la loi de Carreau. *Numer. Math.*, 58(1):35–49, 1990.
- [55] J.W. Barrett and W.B. Liu. Finite element error analysis of a quasi-Newtonian flow obeying the Carreau or power law. *Numer. Math.*, 64(4):433–453, 1993.
- [56] C. Taylor and P. Hood. A numerical solution of the navier-stokes equations using the finite element technique. *Comp. Fluids*, 1(1):73–100, 1973.
- [57] D. J. Smith, E. A. Gaffney, H. Gadêlha, N. Kapur, and J. C. Kirkman-Brown. Bend propagation in the flagella of migrating human sperm, and its modulation by viscosity. *Cell Motil. Cytoskel.*, 66(4):220–236, 2009.
- [58] J. J. L. Higdon. A hydrodynamic analysis of flagellar propulsion. *J. Fluid Mech.*, 90:685–711, 1979.
- [59] F. Bashforth and J. C. Adams. *An attempt to test the theories of capillary action: by comparing the theoretical and measured forms of drops of fluid*. Cambridge Univ. Pr., 1883.
- [60] A. Iserles. *A first course in the numerical analysis of differential equations*. Cambridge Univ. Pr., 2009.
- [61] J. H .E. Cartwright, O. Piro, and I. Tuval. Fluid dynamics in developmental biology: moving fluids that shape ontogeny. *HFSP Journal*, 3(2):77–93, 2009.